INTERNATIONAL JOURNAL FOR NUMERICAL METHODS IN FLUIDS
Int. J. Numer. Meth. Fluids 2008; **57**:1227–1248
Published online 14 April 2008 in Wiley InterScience (www.interscience.wiley.com). DOI: 10.1002/fld.1782

Enhancement of fixed-grid methods towards complex fluid–structure interaction applications

Axel Gerstenberger and Wolfgang A. Wall*, †

Chair for Computational Mechanics, Technische Universität München, Boltzmannstr. 15, 85747 Garching, Germany

SUMMARY

Fixed-grid methods for moving interface problems offer a number of attractive properties and have therefore gained quite some popularity in recent time. However, moving mesh approaches still have their advantages when the physical problem requires special treatment or accurate representation of the interface. This is, for example, the case in complex fluid–structure interaction (FSI) problems when state-of-the-art boundary layer meshing is essential. This paper explores two enhancements of fixed-grid methods that allow the improved solution of such complex FSI problems. The two enhancements are a straightforward approach based on local adaptivity and a hybrid method that combines ideas from fixed-grid methods and arbitrary Lagrangean–Eulerian formulations. Although both enhancements could be used with most available fixed-grid approaches they are given here against the background of a recently developed extended finite element method (XFEM)/Lagrange multiplier (LM) (*Comp. Meth. Appl. Mech. Eng.* 2007. DOI: 10.1016/j.cma.2007.07.002) fixed-grid method. It is shown that the hybrid scheme perfectly fits into the presented XFEM/LM framework in a consistent way. Copyright © 2008 John Wiley & Sons, Ltd.

Received 28 September 2007; Revised 27 December 2007; Accepted 2 January 2008

KEY WORDS: fluid–structure interaction; extended finite element method; fixed grid; domain decomposition; Lagrange multiplier; adaptivity

1. INTRODUCTION

Fixed-grid approaches can be an interesting option when dealing with fluid–structure interaction (FSI) involving large deformation of the structure. Hence, they have recently gained increasing attention [1]. And it is clear that this is an interesting class of problems, since often when interaction effects are essential this comes along with large structural deformations. However, many available

*Correspondence to: Wolfgang A. Wall, Chair for Computational Mechanics, Technische Universität München, Boltzmannstr. 15, 85747 Garching, Germany.
†E-mail: wall@lnm.mw.tum.de

Contract/grant sponsor: Deutsche Forschungsgemeinschaft

approaches (both in research as well as in commercial codes) lack robustness in this situation. One big motivation for our research in this field is the desire to develop robust and efficient methods for general FSI problems that pose no limitations to models and approaches in the individual fields.

It is necessary to properly resolve flow features around the structural surface, where boundary layers, flow separation and re-attachment occur. In addition, usually the structural deformation and shape determine the flow pattern surrounding it. An inaccurate resolution may corrupt the entire simulation. It is crucial to resolve or adequately deal with these features, since otherwise the coupled simulation will not be able to predict the physical solution.

The essential feature of arbitrary Lagrangean–Eulerian (ALE)-based methods is that the fluid field is formulated and solved on a deforming grid. This grid deforms with the structure at the interface and then the grid deformation is extended into the fluid field. Hence, the position of the structure within the fluid domain is known and a fine mesh can be constructed near the interface. As long as this mesh stays intact—usually only for small deformations and specific applications—boundary layers and other flow features near the surface are treated accurate and efficient. For an overview of such techniques, see, e.g. [2]. However, if large and complex motion of the surface occurs, such optimal surface meshes are often difficult to preserve.

In 'pure' fixed-grid methods, the entire fluid domain is described by a fixed Eulerian fluid formulation that is commonly used in fluid problems without moving interfaces. They do not have any moving fluid meshes at all. The interface is described either explicitly, using some kind of Lagrangian interface markers or a Lagrangian structural discretization, or implicitly, using, e.g. level-set functions on the fixed fluid grid. See [3] for an overview on prominent fixed-grid methods.

'Pure' fixed-grid methods in principle allow for unlimited deformation of the structure. In addition, no extra computational costs for mesh movement and mesh smoothing are required. However, unlike in ALE methods, an adequate mesh cannot be constructed beforehand, since the position of the fluid–structure interface is usually not known *a priori*. Hence, for pure fixed-grid methods special care is necessary to create an appropriate mesh that allows for reliable simulation of complex problems.

In this paper, we propose and discuss two different techniques to improve this situation. The first approach is a rather straightforward usage of adaptivity. It is based on local, adaptive mesh refinement and coarsening combined with error estimator-based and/or heuristics-based refinement indicators.

Our second—and currently our favorite—proposal to improve the accuracy/efficiency of fixed-grid methods is to use a hybrid approach combining fixed-grid and ALE techniques. It essentially adds a surface layer of deformable fluid elements with an ALE formulation to the structural surface. Such a fluid patch would capture the near surface flow with an appropriate fine mesh, which is then coupled to a coarse fixed Eulerian background mesh.

For demonstration, the techniques are introduced with a recently proposed Extended Finite Element Method/Lagrange multiplier (XFEM/LM)-based method for FSI [4]. This method addressed a number of general challenges in fixed-grid methods, namely an accurate interface treatment and a proper separation of physical and fictitious flow fields encountered in fixed-grid methods. Of course, the ideas presented in this paper are not limited to XFEM-based methods or FSI problems. They can easily be applied to other existing fixed-grid methods and to problems including free surface flow, two-phase flow or solidification and melting processes to name a few.

The paper is structured as follows: The general FSI problem is stated in Section 2. As a service to the reader, the fluid domain decomposition using XFEM and the direct fixed-grid structure coupling from [4] is reviewed in Section 3. Based on this review we sketch a possible adaptive scheme

DOI: 10.1002/fld

for fixed-grid methods in Section 4 and propose a hybrid scheme in Section 5 that combines the presented XFEM approach with ALE methods. For demonstration of the enhanced fluid solution near the interface, we illustrate the key features for selected fluid examples in Section 6. A comparison between a pure ALE and an adaptive XFEM/LM FSI computation further validates the adaptive approach. Finally, some concluding remarks are given.

2. STATEMENT OF COUPLED FLUID–STRUCTURE PROBLEM

A general FSI problem statement consists of the description of fluid and solid fields, appropriate fluid–structure interface conditions at the common interface and conditions for the remaining boundaries, respectively. Large parts of the paper deal with the fixed fluid field treatment, therefore, we avoid the superscript $(\cdot)^{\mathrm{f}}$ whenever the context allows a clear distinction to other variables.

2.1. Fluid

For a viscous, isothermal and incompressible flow within the fluid domain Ω^{f} (with position vector $\mathbf{x}$), the conservation of momentum is stated as

$$\rho^{\mathrm{f}}\frac{\mathrm{D}\mathbf{u}}{\mathrm{D}t}=\nabla\cdot\boldsymbol{\sigma}^{\mathrm{f}}+\rho^{\mathrm{f}}\mathbf{b}^{\mathrm{f}}\quad\forall\mathbf{x}\in\Omega^{\mathrm{f}} \tag{1}$$

Here, the material time derivative of the fluid velocity $\mathbf{u}(\mathbf{x},t)$ times the fluid density ρ^{f} is balanced by the divergence of the Cauchy stress tensor $\boldsymbol{\sigma}^{\mathrm{f}}$ and external, velocity-independent volumetric forces $\mathbf{b}^{\mathrm{f}}$. For brevity, the volumetric forces are omitted in the subsequent derivation; however, they are included in the actual implementation and their treatment poses no additional difficulties. Mass conservation for an incompressible fluid is stated as

$$\nabla\cdot\mathbf{u}=0 \tag{2}$$

We use the Newtonian material law, which defines the internal stress tensor $\boldsymbol{\sigma}^{\mathrm{f}}$ as

$$\boldsymbol{\sigma}^{\mathrm{f}}=-p\mathbf{I}+2\mu\boldsymbol{\varepsilon}(\mathbf{u}) \tag{3}$$

It is composed of pressure p and a product of the dynamic viscosity denoted as μ and the strain rate tensor $\boldsymbol{\varepsilon}$ given by

$$\boldsymbol{\varepsilon}(\mathbf{u})=\tfrac{1}{2}(\nabla\mathbf{u}+(\nabla\mathbf{u})^{\mathrm{T}}) \tag{4}$$

The specific form of the material time derivative depends on the choice of the reference system that is employed to formulate the problem. The choice of a specific reference system is inspired by the way the moving interface is treated. There are basically three alternative reference systems: the Eulerian, the Lagrangian and the ALE formulation. For the fixed background grid, an Eulerian formulation is used. In this case, the material time derivative is given as the sum of a local time derivative plus a convective term. Hence, the momentum equation reads as

$$\rho^{\mathrm{f}}\dot{\mathbf{u}}=\rho^{\mathrm{f}}\left.\frac{\partial\mathbf{u}}{\partial t}\right|_{\mathbf{x}}=-\rho^{\mathrm{f}}\mathbf{u}\cdot\nabla\mathbf{u}-\nabla p+2\mu\nabla\cdot\boldsymbol{\varepsilon}(\mathbf{u}) \tag{5}$$

$$\nabla\cdot\mathbf{u}=0 \tag{6}$$

DOI: 10.1002/fld

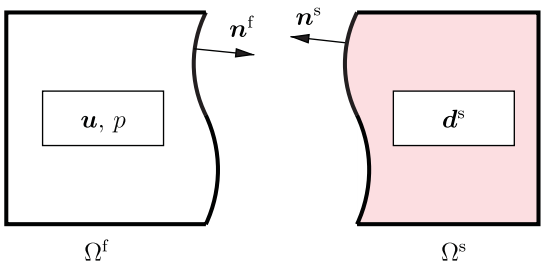

Figure 1. Fluid–structure system with normal vectors $\mathbf{n}^s$, $\mathbf{n}^f$ and field variables.

where the dot over the velocity indicates a partial derivative with respect to time. For the ALE formulation of the momentum equation, the mesh deformation gives rise to the following expressions for the particle velocity $\mathbf{u}(\mathbf{x},t)$ and the grid velocity $\mathbf{u}^g(\mathbf{x},t)$:

$$\rho^f \dot{\mathbf{u}} = \rho^f \left.\frac{\partial \mathbf{u}}{\partial t}\right|_{\boldsymbol{\chi}} = -\rho^f(\mathbf{u}-\mathbf{u}^g)\cdot\nabla\mathbf{u} - \nabla p + 2\mu\nabla\cdot\boldsymbol{\varepsilon}(\mathbf{u}) \tag{7}$$

$$\nabla\cdot\mathbf{u} = 0 \tag{8}$$

where $\boldsymbol{\chi}$ is the coordinate in the moving mesh reference domain. For more details on time discretization and mesh update techniques, see [5, 6].

The Dirichlet and Neumann fluid boundary conditions at $\Gamma^{f,Neu}$ and $\Gamma^{f,Dir}$ are given as

$$\mathbf{u} = \bar{\mathbf{u}} \quad \forall \mathbf{x} \in \Gamma^{f,Dir} \tag{9}$$

$$\boldsymbol{\sigma}^f \cdot \mathbf{n}^f = \bar{\mathbf{h}}^f \quad \forall \mathbf{x} \in \Gamma^{f,Neu} \tag{10}$$

with the normal vector directions defined as in Figure 1. The bar above a variable indicates that this field is a known or prescribed boundary condition for the fluid computation.

Without considering moving interfaces, the weak form of the Navier–Stokes equation in Eulerian form, after integration by parts, becomes

$$(\mathbf{v}, \rho^f \dot{\mathbf{u}})_{\Omega^f} + (\mathbf{v}, \rho^f \mathbf{u}\cdot\nabla\mathbf{u})_{\Omega^f} + (\nabla\cdot\mathbf{v}, \boldsymbol{\sigma}^f)_{\Omega^f} + (q, \nabla\cdot\mathbf{u})_{\Omega^f} - (\mathbf{v}, \bar{\mathbf{h}}^f)_{\Gamma^{f,Neu}} = 0 \tag{11}$$

Such a formulation is known to show instabilities for two reasons—dominating convection and (inf–sup) unstable pairs of velocity and pressure shape functions. In this work, we use linear and quadratic equal-order shape functions for spatial discretization of velocity and pressure. For the employed GLS-type stabilization, we refer the reader to [4].

2.2. Structure

In most applications, the structure is described using a Lagrangian description formulation, where the material time derivative becomes a simple partial derivative with respect to time, such that

$$\rho^s \frac{\partial^2 \mathbf{d}^s}{\partial t^2} = \nabla\cdot\boldsymbol{\sigma}^s + \rho^s \mathbf{b}^s \tag{12}$$

DOI: 10.1002/fld

with the displacement $\mathbf{d}^{\mathrm{s}}(\mathbf{x},t)$ defined as the difference between the current position $\mathbf{x}$ and the initial position $\mathbf{x}_0$, and $\mathbf{b}^{\mathrm{s}}$ being an external acceleration field acting on the structural domain. The structural velocity $\mathbf{u}^{\mathrm{s}}$ and acceleration $\mathbf{a}^{\mathrm{s}}$ are defined as

$$\mathbf{a}^{\mathrm{s}}=\frac{\partial \mathbf{u}^{\mathrm{s}}}{\partial t}=\frac{\partial^2 \mathbf{d}^{\mathrm{s}}}{\partial t^2} \quad \text{or} \quad \mathbf{a}^{\mathrm{s}}=\dot{\mathbf{u}}^{\mathrm{s}}=\ddot{\mathbf{d}}^{\mathrm{s}} \tag{13}$$

The complete strong form, where we omit the body forces for brevity, can be given by

$$\rho^{\mathrm{s}}\ddot{\mathbf{d}}^{\mathrm{s}}=\nabla\cdot\boldsymbol{\sigma}^{\mathrm{s}} \quad \forall \mathbf{x}\in\Omega^{\mathrm{s}} \tag{14}$$

$$\boldsymbol{\sigma}^{\mathrm{f}}\cdot\mathbf{n}^{\mathrm{f}}=\bar{\mathbf{h}}^{\mathrm{s}} \quad \forall \mathbf{x}\in\Gamma^{\mathrm{s,Neu}} \tag{15}$$

$$\mathbf{d}^{\mathrm{s}}=\bar{\mathbf{d}}^{\mathrm{s}} \quad \forall \mathbf{x}\in\Gamma^{\mathrm{s,Dir}} \tag{16}$$

plus proper initial conditions. The weak form after integration by parts without consideration of the fluid–structure coupling is

$$(\delta\mathbf{d}^{\mathrm{s}},\rho^{\mathrm{s}}\ddot{\mathbf{d}}^{\mathrm{s}})_{\Omega^{\mathrm{s}}}+(\nabla\delta\mathbf{d}^{\mathrm{s}},\boldsymbol{\sigma}^{\mathrm{s}})_{\Omega^{\mathrm{s}}}-(\delta\mathbf{d}^{\mathrm{s}},\bar{\mathbf{h}}^{\mathrm{s}})_{\Gamma^{\mathrm{s,Neu}}}=0 \tag{17}$$

The weak form is discretized using different (hybrid-mixed) element techniques in space and direct time integration schemes. Nonlinearities are handled via a Newton–Raphson scheme. For more details on the structural equations we refer the reader to [4]. For the examples in Section 6, a St-Venant–Kirchhoff material law is used.

2.3. Fluid–structure interface conditions

The main conditions at the interface are the dynamic and kinematic coupling conditions. We assume no mass flow across the interface. Consequently, the normal velocities at the interface have to match as

$$\mathbf{u}\cdot\mathbf{n}^{\mathrm{f}}=-\dot{\mathbf{d}}^{\mathrm{s}}\cdot\mathbf{n}^{\mathrm{s}} \quad \forall \mathbf{x}\in\Gamma^{\mathrm{fsi}} \tag{18}$$

Note the opposite sign due to the different normal vector $\mathbf{n}^{\mathrm{f}}$ and $\mathbf{n}^{\mathrm{s}}$ for fluid and structural domain, respectively (Figure 1). If viscous fluids are considered, there is usually also a matching condition for the tangential velocities, which can be combined with the equation above to obtain the 'no slip' boundary conditions as

$$\mathbf{u}=\dot{\mathbf{d}}^{\mathrm{s}} \quad \forall \mathbf{x}\in\Gamma^{\mathrm{fsi}} \tag{19}$$

The force equilibrium requires the surface traction to be equal as

$$\boldsymbol{\sigma}^{\mathrm{f}}\cdot\mathbf{n}^{\mathrm{f}}=-\boldsymbol{\sigma}^{\mathrm{s}}\cdot\mathbf{n}^{\mathrm{s}} \quad \forall \mathbf{x}\in\Gamma^{\mathrm{fsi}} \tag{20}$$

The position of Γ^{fsi} varies with time and is only defined through the interaction of both fields.

3. THE XFEM/LM-BASED APPROACH FOR FIXED-GRID APPROACHES

This section illustrates the XFEM- and LM-based approach, which was described by the authors in the context of FSI in [4].

DOI: 10.1002/fld

3.1. Definition of the fluid problem

In pure fixed-grid methods, the moving surface crosses elements of the fixed background fluid grid. Hence, there is no explicit fluid mesh surface for the background grid to which one can couple the moving surface. It has been shown in [4] how a 3-field approach is advantageous, since it creates an explicit interface discretization Γ^{i} such that the coupling between interface grid and the moving structure surface coupling remains untouched from the fixed fluid treatment.

The moving domain does not have to be a structural domain. Any fully or partially submersed domain Ω^{sub} could be coupled this way. Hence, we will assume no knowledge on the physics of the moving domain for this section. Given the submersed domain Ω^{sub}, we define a domain Ω that contains the fluid domain Ω^{f} completely and extends into the submersed domain Ω^{sub}. The 'wet' surface of Ω^{sub} becomes an internal interface that separates Ω into two subdomains Ω^{+} and Ω^{-}, where Ω^{+} corresponds to the *physical* fluid domain Ω^{f}, and Ω^{-} is the remaining domain-filling Ω. The flow field in Ω^{-} is entirely *fictitious* with no physical meaning to the coupled problem.

The principle setup of the coupling between the interface and the fixed background mesh is depicted in Figure 2. For easier reference, we define two additional names for the boundary Γ^{i}, namely Γ^{+} and Γ^{-}, depending on whether functions are evaluated approaching Γ^{i} from Ω^{+} or Ω^{-}, respectively. For the remainder of this section we assume that the interface displacement $\bar{\mathbf{d}}^{\mathrm{i}}$ and velocity $\bar{\mathbf{u}}^{\mathrm{i}}$ to be known.

The material movement in the physical domain and the interface are coupled by

$$\mathbf{u} = \bar{\mathbf{u}}^{\mathrm{i}} \quad \forall \mathbf{x} \in \Gamma^{\mathrm{i}} \tag{21}$$

However, the kinematic conditions along the interface are useful boundary conditions only for Ω^{+}. For Ω^{-}, the entire boundary shall be a Neumann boundary with zero traction. Hence, we have two boundary conditions along Γ^{i} as

$$\mathbf{u} = \bar{\mathbf{u}}^{\mathrm{i}} \quad \forall \mathbf{x} \in \Gamma^{+} \tag{22}$$

$$\boldsymbol{\sigma}^{\mathrm{f}} \cdot \mathbf{n} = \mathbf{0} \quad \forall \mathbf{x} \in \Gamma^{-} \tag{23}$$

Fulfilling both conditions (22) and (23) along Γ^{i} requires us to introduce a discontinuous velocity and stress field, which will be done during the spatial discretization process. In Ω^{+} the initial conditions are given as $\mathbf{u}(\mathbf{x}, t=0) = \mathbf{u}^{0}$ and $p(\mathbf{x}, t=0) = p^{0}$ while in Ω^{-} zero initial velocity and pressure are applied. Body forces, if present, are only applied to Ω^{+}. With this set of boundary

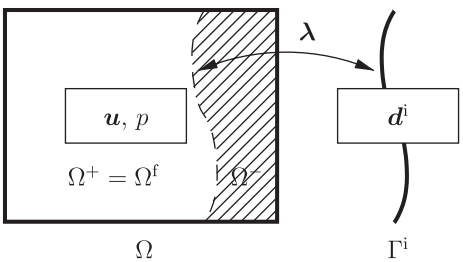

Figure 2. Fluid part of the FSI problem: Γ^{i} separates the computational fluid domain Ω in a physical fluid domain Ω^{+} corresponding to Ω^{f} and the 'fictitious' fluid domain Ω^{-}. The Lagrange multiplier field $\boldsymbol{\lambda}$ connects the interface and fixed-grid velocity.

DOI: 10.1002/fld

and initial conditions and a properly decoupled flow field between Ω^+ and Ω^-, there will be zero velocity and pressure in Ω^- at all times. Hence, one goal—an entirely switched off fluid domain—is achieved in that way.

3.2. Fluid discretization in time

For simplicity of presentation, we only describe the one-step-θ method for time discretization. Here, the acceleration $\dot{\mathbf{u}}$ is defined as a combination of the acceleration at the new and the old time step

$$\frac{\mathbf{u}^{n+1}-\mathbf{u}^n}{\Delta t}=\theta\dot{\mathbf{u}}^{n+1}+(1-\theta)\dot{\mathbf{u}}^n \tag{24}$$

Similarly, the pressure is discretized in time as

$$p^{n+\theta}=\theta p^{n+1}+(1-\theta)p^n \tag{25}$$

Now $\dot{\mathbf{u}}^{n+1}$ can be replaced by the right-hand side of Equation (5) evaluated at the new time step $n+1$

$$\mathbf{u}^{n+1}+\Delta t\theta\left[\mathbf{u}\cdot\nabla\mathbf{u}-\frac{1}{\rho^{\mathrm{f}}}\nabla\cdot\boldsymbol{\sigma}^{\mathrm{f}}\right]^{n+1}=\mathbf{u}^n+\Delta t(1-\theta)\dot{\mathbf{u}}^n \tag{26}$$

in Ω. To complete the time-discrete strong form for the fluid flow in Ω^+ and Ω^-, we also require

$$\nabla\cdot\mathbf{u}^{n+1}=0 \tag{27}$$

3.3. Weak form of the time-discrete flow equations

The weak form is developed by multiplying Equations (26) and (27) with the velocity and pressure test functions $\mathbf{v}$ and q, respectively

$$\begin{aligned}&[(\mathbf{v},\rho^{\mathrm{f}}\mathbf{u})_\Omega+\Delta t\theta\{(\mathbf{v},\rho^{\mathrm{f}}\mathbf{u}\cdot\nabla\mathbf{u}-\nabla\cdot\boldsymbol{\sigma}^{\mathrm{f}})_\Omega+(q,\nabla\cdot\mathbf{u})_\Omega-(\delta\boldsymbol{\lambda},\mathbf{u}-\bar{\mathbf{u}}^{\mathrm{i}})_{\Gamma^+}\}]^{n+1}\\&\quad=(\mathbf{v},\rho^{\mathrm{f}}\mathbf{u}^n)_\Omega+\Delta t(1-\theta)(\mathbf{v},\rho^{\mathrm{f}}\dot{\mathbf{u}}^n)_\Omega\end{aligned} \tag{28}$$

The fluid–interface condition (22) is enforced weakly by testing the condition with a test function $\delta\boldsymbol{\lambda}(\mathbf{x})$ along the interface. This is necessary, since we cannot apply Equation (22) directly as Dirichlet conditions due to the non-fitting fluid and interface meshes. It should be clear from Equation (28) that the coupling condition is weakly enforced at t^{n+1} at the t^{n+1} location of the interface Γ^{i}.

Already from a dimensional analysis we see that $\delta\boldsymbol{\lambda}$ has to be a kind of virtual traction vector. In our particular setup, where velocities and pressure jump from zero in Ω^- to their physical values in Ω^+, the traction corresponds to the reaction force, as if an ordinary domain boundary would be at this place. Therefore, on Γ^+, $\boldsymbol{\sigma}^{\mathrm{f}}\cdot\mathbf{n}^{\mathrm{f}}$ can be defined as the Lagrange multiplier field $\boldsymbol{\lambda}$ such that integration by parts of the stress term yields

$$-(\mathbf{v},\nabla\cdot\boldsymbol{\sigma}^{\mathrm{f}})_\Omega=-(\mathbf{v},\bar{\mathbf{h}}^{\mathrm{f}})_{\Gamma^{\mathrm{f,Neu}}}-(\mathbf{v},\boldsymbol{\lambda})_{\Gamma^+}+(\nabla\cdot\mathbf{v},\boldsymbol{\sigma}^{\mathrm{f}})_\Omega \tag{29}$$

For Dirichlet boundary conditions, the surface integral vanishes due to the vanishing test function. Dirichlet and Neumann conditions away from the interface are employed as usual; therefore, we will not include the Neumann boundary term in the following derivation for the sake of clarity.

DOI: 10.1002/fld

Inserting Equation (29) and reordering Equation (28) for unknown and known expressions, the final weak form is

$$\begin{aligned}&[(\mathbf{v},\rho^{\mathrm{f}}\mathbf{u})_{\Omega}+\Delta t\theta\{(\mathbf{v},\rho^{\mathrm{f}}\mathbf{u}\cdot\nabla\mathbf{u})_{\Omega}+(\nabla\cdot\mathbf{v},\boldsymbol{\sigma}^{\mathrm{f}})_{\Omega}\\&\quad+(q,\nabla\cdot\mathbf{u})_{\Omega}-(\mathbf{v},\boldsymbol{\lambda})_{\Gamma^{+}}-(\delta\boldsymbol{\lambda},\mathbf{u})_{\Gamma^{+}}\}]^{n+1}\\&\quad=(\mathbf{v},\rho^{\mathrm{f}}\mathbf{u}^{n})_{\Omega}+\Delta t(1-\theta)(\mathbf{v},\rho^{\mathrm{f}}\dot{\mathbf{u}}^{n})_{\Omega}-\Delta t\theta(\delta\boldsymbol{\lambda},\bar{\mathbf{u}}^{\mathrm{i},n+1})_{\Gamma^{+}}\end{aligned}\tag{30}$$

As mentioned in Section 2, the fluid equations need stabilizing terms for dominating convection and equal order, bi-quadratic interpolation as used in the following. Note that we do not employ any stabilization terms on the Lagrange multiplier expression $(\mathbf{v},\boldsymbol{\lambda})_{\Gamma^{+}}$.

3.4. Fluid discretization in space

As should be clear by now, the fluid–structure interface is generally not aligned with fluid element surfaces. Consequently, we need to find a way to represent a jump in the primary variables, namely velocity and pressure. Furthermore, also the derivatives have to be discontinuous, since the stress field is discontinuous as well.

The XFEM [7, 8] allows one to enrich the standard approximation function space to represent strong or weak discontinuities. For instance, the velocity field could be enriched as

$$\mathbf{u}^{h}(\mathbf{x},t)=\sum_{I}N_{I}(\mathbf{x})(\tilde{\mathbf{u}}_{I}(t)+\psi(\mathbf{x},t)\hat{\mathbf{u}}_{I}(t))\tag{31}$$

Here, $\tilde{\mathbf{u}}_{I}(t)$ represent the standard nodal degrees of freedom at node I, while additional degrees of freedom $\hat{\mathbf{u}}_{I}(t)$ multiplied by a properly chosen enrichment function $\psi(\mathbf{x},t)$ are used to enhance the solution. It is important to note the partition of unity character of this approximation [9].

The choice of the enrichment function depends on the character of the interface conditions. For our interface problem, we have a jump in velocity and stress terms (including pressure) from their physical values in Ω^{+} to zero velocity and stress fields in Ω^{-}. Hence, for our purpose the enrichment function is defined as a step function $H(\mathbf{x},t)$

$$\psi(\mathbf{x},t)=H(\mathbf{x},t)=\begin{cases}+1 & \forall\mathbf{x}\in\Omega^{+}(t)\\ 0 & \forall\mathbf{x}\in\Omega^{-}(t)\end{cases}\tag{32}$$

Along Γ^{i}, both velocity and pressure are discontinuous and enriched with H. The complete discretization for trial and test functions with equal-order ansatz functions for velocity and pressure is given as

$$\mathbf{u}^{h,n+1}(\mathbf{x})=\sum_{I}N_{I}(\mathbf{x})(\tilde{\mathbf{u}}_{I}^{n+1}+H^{n+1}(\mathbf{x})\hat{\mathbf{u}}_{I}^{n+1})\tag{33}$$

$$\mathbf{v}^{h}(\mathbf{x})=\sum_{I}N_{I}(\mathbf{x})(\tilde{\mathbf{v}}_{I}+H^{n+1}(\mathbf{x})\hat{\mathbf{v}}_{I})\tag{34}$$

and

$$p^{h,n+1}(\mathbf{x})=\sum_{I}N_{I}(\mathbf{x})(\tilde{p}_{I}^{n+1}+H^{n+1}(\mathbf{x})\hat{p}_{I}^{n+1})\tag{35}$$

$$q^{h}(\mathbf{x})=\sum_{I}N_{I}(\mathbf{x})(\tilde{q}_{I}+H^{n+1}(\mathbf{x})\hat{q}_{I})\tag{36}$$

DOI: 10.1002/fld

The superscript 'h' indicates the discretized field function. Across the interface, derivatives of such discontinuous approximation result in Dirac functions, which has been identified and taken into account as traction vector $\boldsymbol{\lambda}$ in Equation (30).

Higher-order shape functions, e.g. for the bi-quadratic 9-node fluid element used in the examples, are treated with no additional effort making this approach capable for consistent low- and high-order finite element (FE) approximations.

If more than one interface crosses one fluid element, simply more enrichments can be used, using one enrichment for each interface. The additional unknowns $\hat{\mathbf{u}}_I^{\mathbf{1}}, \hat{\mathbf{u}}_I^{\mathbf{2}}, \ldots$ and enrichment functions $H^{\mathbf{1}}, H^{\mathbf{2}}, \ldots$ are summed as

$$\mathbf{u}^h(\mathbf{x}) = \sum_I N_I(\mathbf{x})(\tilde{\mathbf{u}}_I + H^{\mathbf{1}}(\mathbf{x})\hat{\mathbf{u}}_I^{\mathbf{1}} + H^{\mathbf{2}}(\mathbf{x})\hat{\mathbf{u}}_I^{\mathbf{2}} + \cdots) \tag{37}$$

with the time dependence omitted for brevity. This feature allows very thin structures—even thinner than one underlying fluid element—as well as possible extensions to contact problems of submersed structures.

Along the interface Γ^{i}, the Lagrange multiplier field and the corresponding test functions are discretized as

$$\boldsymbol{\lambda}^h = \sum_I N_I^{\mathrm{i}} \boldsymbol{\lambda}_I \quad \text{and} \quad \delta\boldsymbol{\lambda}^h = \sum_I N_I^{\mathrm{i}} \delta\boldsymbol{\lambda}_I \tag{38}$$

The same shape functions N_I^{i} are also used to discretize the interface velocities and displacements

$$\mathbf{u}^{\mathrm{i},h} = \sum_I N_I^{\mathrm{i}} \mathbf{u}_I^{\mathrm{i}} \quad \text{and} \quad \mathbf{d}^{\mathrm{i},h} = \sum_I N_I^{\mathrm{i}} \delta\mathbf{d}_I^{\mathrm{i}} \tag{39}$$

The choice of appropriate shape functions N_I^{i} are influenced by the background fluid discretization. Inappropriate choices lead to oscillations or locking due to violation of the inf–sup condition. A recent discussion of applying Dirichlet boundary conditions in the context of XFEM can be found in [10]. For the implementation used in this paper, we used bi-quadratic ansatz functions N_I for fluid velocity and pressure and linear ansatz function N_I^{i} for the interface variables, where no oscillation and locking were observed. For further details on enrichment strategies, the construction of the interface mesh and the numerical integration, see [4].

3.5. Solution of the fluid equations

The complete fluid–interface system including the Lagrange multiplier formulation becomes

$$\begin{bmatrix} \mathbf{A}_{uu} & \mathbf{A}_{up} & -\Delta t\theta \mathbf{M}_\lambda^{\mathrm{T}} \\ \mathbf{A}_{pu} & \mathbf{A}_{pp} & \mathbf{0} \\ -\Delta t\theta \mathbf{M}_\lambda & \mathbf{0} & \mathbf{0} \end{bmatrix} \begin{bmatrix} \mathbf{u} \\ \mathbf{p} \\ \boldsymbol{\lambda} \end{bmatrix} = \begin{bmatrix} \mathbf{f}^{\mathrm{rhs}} \\ \mathbf{0} \\ -\Delta t\theta \mathbf{D}_\lambda \bar{\mathbf{u}}^{\mathrm{i}} \end{bmatrix} \tag{40}$$

where

$$\mathbf{D}_\lambda\colon \quad D_{IJij} = \int_{\Gamma^+} N_I^{\mathrm{i}} N_J^{\mathrm{i}} \, \mathrm{d}\mathbf{x} \delta_{ij} \tag{41}$$

DOI: 10.1002/fld

and

$$\mathbf{M}_\lambda: \quad M_{KLij} = \int_{\Gamma^+} N_K^{\mathrm{i}} \mathscr{P}^{\mathrm{f}} N_L^{\mathrm{f}} \, \mathrm{d}\mathbf{x} \delta_{ij} \tag{42}$$

with δ_{ij} being the Kronecker-δ, i.e. $\delta_{ij} = 1$ if $i = j$, else 0. The projection $\mathscr{P}^{\mathrm{f}}$ connects between variables on the background grid and the interface mesh, which results in a rectangular submatrix $\mathbf{M}_\lambda$. The submatrices $\mathbf{A}_{uu}$, $\mathbf{A}_{up}$, $\mathbf{A}_{pu}$ and $\mathbf{A}_{pp}$ denote the standard matrices arising in stabilized FE formulations of the Navier–Stokes equation.

3.6. Direct fixed-grid fluid–structure coupling

The coupled fluid–interface system is now directly coupled to a structural surface as shown in Figure 3. The interface mesh generally does not match the surface discretization of the structure. Hence, we introduced a 3-field approach in [4], where we adopted Mortar methods for non-matching grids, see [11–13].

The kinematic matching condition implies that displacements of the interface and structural surface are the same at all times. Hence, instead of Equation (19), we can state

$$\mathbf{d}^{\mathrm{s}} = \mathbf{d}^{\mathrm{i}} \quad \forall \mathbf{x} \in \Gamma^{\mathrm{i}} \tag{43}$$

In the Mortar method, the kinematic matching condition (43) is enforced weakly by using a Lagrange multiplier field $\boldsymbol{\mu}$, which can be identified as a surface traction.

The weak form of the structural momentum equation (17) after integration by parts including the interface condition (43) reads as

$$(\delta\mathbf{d}^{\mathrm{s}}, \rho^{\mathrm{s}} \ddot{\mathbf{d}}^{\mathrm{s}})_{\Omega^{\mathrm{s}}} + (\nabla \delta\mathbf{d}^{\mathrm{s}}, \boldsymbol{\sigma}^{\mathrm{s}})_{\Omega^{\mathrm{s}}} - (\delta\mathbf{d}^{\mathrm{s}}, \boldsymbol{\mu})_{\Gamma^{\mathrm{i}}} - (\delta\boldsymbol{\mu}, \mathbf{d}^{\mathrm{s}} - \mathbf{d}^{\mathrm{i}})_{\Gamma^{\mathrm{i}}} = 0 \tag{44}$$

For Dirichlet boundary conditions, the surface integral vanishes due to the vanishing test function. Neumann conditions are applied by letting $\boldsymbol{\sigma}^{\mathrm{s}} \cdot \mathbf{n}^{\mathrm{s}} = \bar{\mathbf{h}}^{\mathrm{s}}$; however, the implementation of Neumann conditions is straightforward and will not be discussed further for brevity.

Discretization of the structural displacement is done as usual using shape functions N_I^{s}

$$\mathbf{d}^{\mathrm{s},h} = \sum_I N_I^{\mathrm{s}} \mathbf{d}_I^{\mathrm{s}} \quad \text{and} \quad \delta\mathbf{d}^{\mathrm{s},h} = \sum_I N_I^{\mathrm{s}} \delta\mathbf{d}_I^{\mathrm{s}} \tag{45}$$

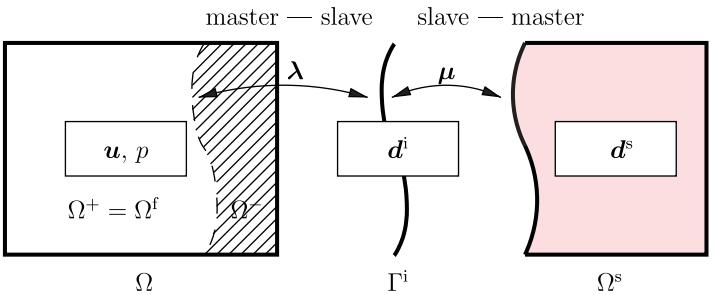

Figure 3. Coupled problem with three fields, along with variables living on each domain and the Lagrange multiplier fields.

DOI: 10.1002/fld

The Lagrange multiplier is discretized with the shape functions and node set of the slave side, namely the interface. Then, trial and test functions of the Lagrange multiplier field are discretized as

$$\boldsymbol{\mu}^h = \sum_I N_I^{\mathrm{i}} \boldsymbol{\mu}_I \quad \text{and} \quad \delta\boldsymbol{\mu}^h = \sum_I N_I^{\mathrm{i}} \delta\boldsymbol{\mu}_I \tag{46}$$

Furthermore, the interface may be curved and surface elements do not necessarily coincide with the interface elements. Consequently, we need a projection $\mathscr{P}^{\mathrm{s}}$ [13] to integrate the weak form

$$\delta W^{\mathrm{s}} = 0 = \int_{\Gamma^{\mathrm{i}}} \delta\boldsymbol{\mu}^h (\mathscr{P}^{\mathrm{s}} \mathbf{d}^{\mathrm{s},h} - \mathbf{d}^{\mathrm{i},h})\, \mathrm{d}\mathbf{x} \tag{47}$$

The virtual work δW^{s} done by the virtual force $\delta\boldsymbol{\mu}^h$ allows one to define two coupling matrices $\mathbf{M}_\mu$ and $\mathbf{D}_\mu$ as

$$0 = \delta\mu_{Ii} \left[\underbrace{\int_{\Gamma^{\mathrm{i}}} N_I^{\mathrm{i}} \mathscr{P}^{\mathrm{s}} N_J^{\mathrm{s}}\, \mathrm{d}\mathbf{x}}_{\mathbf{M}_\mu} d_{Ji}^{\mathrm{s}} - \underbrace{\int_{\Gamma^{\mathrm{i}}} N_I^{\mathrm{i}} N_K^{\mathrm{i}}\, \mathrm{d}\mathbf{x}}_{\mathbf{D}_\mu} d_{Ki}^{\mathrm{i}} \right] \tag{48}$$

The corresponding reaction force along Γ^{i} can be derived from the traction balance along the interface. In the XFEM approach, the Lagrange multiplier field $\boldsymbol{\mu}$ was recognized as the surface traction field acting on the structural surface. Expressing $(\delta\mathbf{d}^{\mathrm{s}}, \boldsymbol{\mu})_{\Gamma^{\mathrm{i}}}$ in its discretized form we obtain

$$(\delta\mathbf{d}^{\mathrm{s},h}, \boldsymbol{\mu}^h)_{\Gamma^{\mathrm{i}}} = \delta d_{Ii}^{\mathrm{s}} \underbrace{\int_{\Gamma^{\mathrm{i}}} \mathscr{P}^{\mathrm{s}} N_I^{\mathrm{s}} N_J^{\mathrm{i}}\, \mathrm{d}\mathbf{x}}_{\mathbf{M}_\mu^{\mathrm{T}}} \mu_{Ji} \tag{49}$$

Now the Neumann nodal force vector can simply be expressed in the matrix notation as

$$\mathbf{f}^{\mathrm{s,fsi}} = \mathbf{M}_\mu^{\mathrm{T}} \boldsymbol{\mu} \tag{50}$$

For structural time integration, a β-Newmark scheme [14, 15] is employed with parameters set to $\beta = 0.25$ and $\gamma = 0.5$ making it an implicit time integration scheme. With the effective tangent stiffness $\mathbf{A}_d$ defined from the mass matrix $\mathbf{M}$ and the stiffness matrix $\mathbf{K}$ as

$$\mathbf{A}_d = \frac{1}{\beta \Delta t^2} \mathbf{M} - \mathbf{K} \tag{51}$$

and the effective force $\mathbf{f}^{\mathrm{dyn}}$ representing terms from the old time step as

$$\mathbf{f}^{\mathrm{dyn}} = -\frac{1}{\Delta t^2} \mathbf{M} \mathbf{d}^n + \frac{1-2\beta}{2\beta} \mathbf{M} \ddot{\mathbf{d}}^n \tag{52}$$

the fully discretized structural equations is

$$\mathbf{A}_d \mathbf{d} = \mathbf{f}^{\mathrm{dyn}} + \mathbf{f}^{\mathrm{s,fsi}} \tag{53}$$

Finally, the interface velocity $\mathbf{u}^{\mathrm{i}}$ has to be discretized in time, since displacement $\mathbf{d}^{\mathrm{i}}$ and velocity $\mathbf{u}^{\mathrm{i}}$ of the surface are connected by the simple differential equation $\dot{\mathbf{d}}^{\mathrm{i}} = \mathbf{u}^{\mathrm{i}}$. For simplicity, we again use the one-step-θ method. The interface velocity at the new time step is then calculated from the

DOI: 10.1002/fld

interface displacements as

$$\mathbf{u}^{\mathrm{i},n+1} = \frac{1}{\Delta t \theta^{\mathrm{i}}}(\mathbf{d}^{\mathrm{i},n+1} - \mathbf{d}^{\mathrm{i},n}) - \frac{1-\theta^{\mathrm{i}}}{\theta^{\mathrm{i}}}\mathbf{u}^{\mathrm{i},n} \tag{54}$$

For the presented calculations, $\theta^{\mathrm{i}} = 0.5$ has been used. Note the discussion on stability in [4, 5]. With a predictor defined as $\mathbf{d}^{\mathrm{i,pred}} = \Delta t(1-\theta^{\mathrm{i}})\mathbf{u}^{\mathrm{i},n} + \mathbf{d}^{\mathrm{i},n}$, we can pose the complete coupled discrete system as

$$\begin{bmatrix} \mathbf{A}_{uu} & \mathbf{A}_{up} & -\Delta t\theta\mathbf{M}_{\lambda}^{\mathrm{T}} & \mathbf{0} & \mathbf{0} & \mathbf{0} \\ \mathbf{A}_{pu} & \mathbf{A}_{pp} & \mathbf{0} & \mathbf{0} & \mathbf{0} & \mathbf{0} \\ -\Delta t\theta^{\mathrm{i}}\mathbf{M}_{\lambda} & \mathbf{0} & \mathbf{0} & \mathbf{D}_{\lambda} & \mathbf{0} & \mathbf{0} \\ \mathbf{0} & \mathbf{0} & \mathbf{D}_{\lambda}^{\mathrm{T}} & \mathbf{0} & \mathbf{D}_{\mu}^{\mathrm{T}} & \mathbf{0} \\ \mathbf{0} & \mathbf{0} & \mathbf{0} & \mathbf{D}_{\mu} & \mathbf{0} & -\mathbf{M}_{\mu} \\ \mathbf{0} & \mathbf{0} & \mathbf{0} & \mathbf{0} & -\mathbf{M}_{\mu}^{\mathrm{T}} & \mathbf{A}_{d} \end{bmatrix} \begin{bmatrix} \mathbf{u} \\ \mathbf{p} \\ \boldsymbol{\lambda} \\ \mathbf{d}^{\mathrm{i}} \\ \boldsymbol{\mu} \\ \mathbf{d}^{\mathrm{s}} \end{bmatrix} = \begin{bmatrix} \mathbf{f}^{\mathrm{rhs}} \\ \mathbf{0} \\ \mathbf{D}_{\lambda}\mathbf{d}^{\mathrm{i,pred}} \\ \mathbf{0} \\ \mathbf{0} \\ \mathbf{f}^{\mathrm{dyn}} \end{bmatrix} \tag{55}$$

An iterative approach for the solution of the coupled problem is given in [4].

4. ADAPTIVE FIXED-GRID METHODS

The first and straightforward idea to improve the situation near the fluid–structure interface is to use adaptive schemes. This is necessary since the structure may strongly influence the flow field and it is necessary to accurately capture boundary layers, separation and re-attachment of the flow to the moving interface. In this paper, we concentrate on *h*-adaptivity while extensions could be made to use *hp*-FE methods, see, e.g. [16] and references therein.

An *h*-adaptive scheme essentially consists of two steps: finding an appropriate refinement/coarsening indicator based on heuristics or some kind of global or local error estimate and creating an adaptive mesh.

For fixed-grid methods, a refinement indicator could be as simple to refine all elements within a given distance from the interface and make a smooth transition towards coarser elements. If, for example, the size of the boundary layer can be predicted *a priori*, this approach is straightforward. However, if flow features develop not only near the interface and are generally not predictable such heuristics are hardly sufficient. Hence, defining the refinement indicator based on some global or local error seems more general and preferable. See [17–20] and references therein for a more complete overview on this topic.

In our computations, we use a combination of refining by the interface distance and a gradient-based error indicator. The error indicator ε^{e} for each element 'e' is computed from the integral of the absolute value of the shear strain rate jump along the element boundaries Γ^{e} to estimate the smoothness of the computed result

$$\varepsilon^{\mathrm{e}} = \oint_{\Gamma^{\mathrm{e}}} |[u_{x,y}]| \, \mathrm{d}\mathbf{x} \tag{56}$$

Here, $u_{x,y}$ is the gradient of the fluid velocity field. For the results given in the example section, this indicator resolves boundary layers along normal and implicit boundaries very well.

DOI: 10.1002/fld

After indicating, in which area refinement is needed and coarsening can be allowed there are several choices for a refinement strategy, see, e.g. [21] for an overview on refinement techniques. Complete or partial re-meshing based on automatic meshing algorithms does not seem to be a good choice, since fixed-grid FSI methods were introduced precisely to avoid re-meshing due to the deforming interface. Adding re-meshing for accuracy/efficiency seems therefore counterintuitive.

Other approaches allow local refinement by subdividing existing elements into smaller elements. This inevitably introduces hanging nodes, which essentially creates incompatible elements, when coarse and refined elements are neighbors. To obtain a compatible mesh, one can subdivide neighboring elements such that no hanging nodes are left [18, 22]. Another possibility is to constrain nodes on the finer side such that a compatible solution is recovered [13, 16]. The latter approaches can also be used for higher-order *hp*-refinement and multiple hanging nodes.

In our computations involving linear (4-node) and quadratic (8- or 9-node) elements, we use a local refinement strategy based on hanging nodes. The refinement procedure for a 9-node element is depicted in Figure 4. After refinement, there are three nodes of a quadratic line element on the coarse side and five nodes of two quadratic lines on the refined side. Then, the two center nodes of the small elements cannot be chosen freely, since that would introduce an incompatible solution. Instead, their values need to be constrained to the coarser solution.

The relation between unknowns on the refined side u_J^{f} and the coarse side u_I^{c} can be expressed as the following matrix expression:

$$\begin{bmatrix} u_1^{\mathrm{f}} \\ u_2^{\mathrm{f}} \\ u_3^{\mathrm{f}} \\ u_4^{\mathrm{f}} \\ u_5^{\mathrm{f}} \end{bmatrix} = \begin{bmatrix} 1.0 & 0.0 & 0.0 \\ 0.375 & 0.75 & -0.125 \\ 0.0 & 1.0 & 0.0 \\ -0.125 & 0.75 & 0.375 \\ 0.0 & 0.0 & 1.0 \end{bmatrix} \begin{bmatrix} u_1^{\mathrm{c}} \\ u_2^{\mathrm{c}} \\ u_3^{\mathrm{c}} \end{bmatrix} \tag{57}$$

where nodes of the coarse mesh coincide with the fine mesh, the matrix contains simply a 1 to 1 matching, otherwise, it is a sum of several entries. The sum of all entries in one row has to be 1. For linear elements, the connectivity matrix is even simpler

$$\begin{bmatrix} u_1^{\mathrm{f}} \\ u_2^{\mathrm{f}} \\ u_3^{\mathrm{f}} \end{bmatrix} = \begin{bmatrix} 1.0 & 0.0 \\ 0.5 & 0.5 \\ 0.0 & 1.0 \end{bmatrix} \begin{bmatrix} u_1^{\mathrm{c}} \\ u_2^{\mathrm{c}} \end{bmatrix} \tag{58}$$

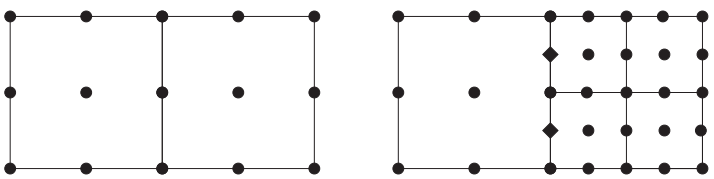

Figure 4. Refinement of quadratic elements using hanging nodes (indicated by diamonds): (a) unrefined elements and (b) refined elements with hanging nodes.

DOI: 10.1002/fld

The matrices can be constructed from simple evaluation of line shape functions or by using a local mortar approach along the interface between a coarse and two small elements Γ^{a}, where the matrix above corresponds to the rectangular matrix

$$0=\int_{\Gamma^{\mathrm{a}}} N_I^{\mathrm{f}} N_J^{\mathrm{c}}\,\mathrm{d}\mathbf{x}\,u_J^{\mathrm{c}}-\int_{\Gamma^{\mathrm{a}}} N_I^{\mathrm{f}} N_K^{\mathrm{f}}\,\mathrm{d}\mathbf{x}\,u_K^{\mathrm{f}} \tag{59}$$

or expressed in matrix notation

$$0=\mathbf{D}\mathbf{u}^{\mathrm{c}}-\mathbf{M}\mathbf{u}^{\mathrm{f}} \tag{60}$$

Hence, the values on the fine grid are calculated as

$$\mathbf{u}^{\mathrm{f}}=\mathbf{D}^{-1}\mathbf{M}\mathbf{u}^{\mathrm{c}} \tag{61}$$

For simplicity of implementation, we allow only one coarse element be connected to two finer elements.

In practice, hanging nodes do not carry unknowns and their values can be established by interpolation from the coarse side. The integration of elements containing hanging nodes remains unchanged compared with elements without hanging nodes. Only the interpolation and assembly process need to be changed. When an element containing a hanging node as one of its nine nodes is processed, it first interpolates the nodal values from the coarser neighbor element. It can then compute residual and tangent stiffness as usual. Finally, the entries of residual and stiffness matrix belonging to the hanging node are added to the nodes on the coarse element entries using Equations (57) or (58).

In summary, *h*-adaptivity based on local element sub-division provides a general applicable way to improve the accuracy of fixed-grid methods. The use of automatic refinement complements the idea of fixed-grid methods, where not much predictions on the structural movement can be made *a priori*. For transient problems involving large motions of the structural surface, mesh updates have to be performed very frequently to follow the implicit interface. If a too small region around the structure is refined, the mesh update and error estimation have to be performed very frequently to follow the motion of the interface. On the other hand, if a too large region is refined, the sheer number of additional elements that are used 'just in case' can be prohibitively high.

In such cases it would be advantageous to have a small layer of fluid elements along the structural surface such that a close to optimal boundary layer mesh is kept at all times. Such an approach is presented in the following section.

5. A HYBRID FIXED-GRID/ALE APPROACH

The second approach to improve fixed-grid methods involves the addition of a deformable fluid domain around the structural surface. In other words, the submersed domain Ω^{sub} is now the union of the structural domain Ω^{s} and the moving fluid grid Ω^{ALE}. Using the deformable fluid patch provides several advantages: the ALE mesh connectivity does not change with time and they can be made more efficient by using stretched elements, e.g. to efficiently resolve boundary layers that have strong gradients usually only normal to the structural surface. In fact, state-of-the-art boundary layer elements can have very large aspect ratios and there is no straightforward way to obtain such an optimal boundary layer mesh by using element subdivision.

DOI: 10.1002/fld

Coupling between moving fluid domain and structure can be handled in the same way as in traditional ALE FSI schemes. The interesting questions are how the intermediate moving grid is coupled to the background grid and how the 'fictitious domain' Ω^{sub} is treated on the background grid.

Such hybrid methods have been used before to enable rigid movement of structures in fluids based on the well-known Chimera technique [1, 23–25]. Recently, a Chimera-like method was developed in [3, 26], which also allowed thick and thin deforming structures. In these approaches, the fixed grid and ALE grid overlapped each other and are solved alternately using iterative schemes. A related, non-overlapping approach is the so-called sliding mesh technique [27], which uses local mesh updates (by simply reconnecting nodes) to connect background and patch mesh.

In the following, we propose another technique that perfectly fits our developed XFEM approach. In particular, instead of coupling the structural domain to the fluid grid as in Section 3, now the ALE grid surface is coupled to the fixed grid and defines the discontinuity in the background grid. The fluid–fluid coupling is developed using the same 3-field approach such that the submersed patch is the union of structural domain and the ALE patch domain $\Omega^{\text{sub}} = \Omega^{\text{s}} \cup \Omega^{\text{ALE}}$. On the fixed grid, the flow in Ω^{sub} is turned off and does not influence the physical flow.

Figure 5 shows how the intermediate ALE mesh is coupled to the structure surface using the Lagrange multiplier field $\boldsymbol{\kappa}$. In the ALE and the fixed mesh the principle unknowns are the same, namely velocity and pressure. Unlike the velocity–displacement coupling in the direct fluid–structure coupling (Section 3), we can express the matching conditions as

$$\mathbf{u} = \mathbf{u}^{\text{ALE}} \quad \forall \mathbf{x} \in \Gamma^{\text{i}} \tag{62}$$

Therefore, we can directly couple the fluid velocities without using an intermediate interface displacement

$$0 = \delta\lambda_{Ii} \left[\underbrace{\int_{\Gamma^{\text{i}}} N_I^{\text{i}} \mathscr{P}^{\text{f}} N_J^{\text{f}} \, \mathrm{d}\mathbf{x}}_{\mathbf{M}_\lambda} u_{Ji}^{\text{f}} + \underbrace{\int_{\Gamma^{\text{i}}} N_I^{\text{i}} \mathscr{P}^{\text{ALE}} N_K^{\text{ALE}} \, \mathrm{d}\mathbf{x}}_{\mathbf{M}_\mu} u_{Ki}^{\text{ALE}} \right] \tag{63}$$

The projections $\mathscr{P}^{\text{f}}$ was defined in Section 3.5 and $\mathscr{P}^{\text{ALE}}$ corresponds to $\mathscr{P}^{\text{s}}$ from Section 3.6.

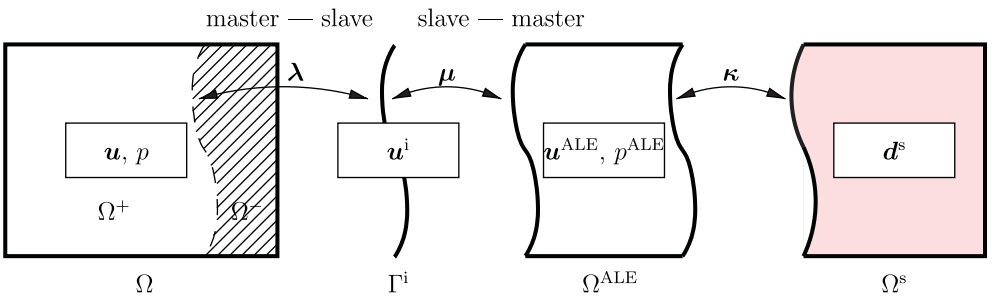

Figure 5. Hybrid approach: a fixed fluid grid and a deforming ALE fluid grid are coupled using the XFEM/Lagrange multiplier approach. The moving ALE grid can in turn be coupled to the structure field. Variables living on each domain and the Lagrange multiplier fields are also shown.

DOI: 10.1002/fld

The time discretization was chosen to be the same for moving and fixed fluid domain, which additionally simplifies the coupling procedure. Replacing the structural equations with the ALE fluid equations, the complete, monolithic weak form is given as

$$
\begin{aligned}
&[(\mathbf{v}, \rho^{\mathrm{f}}\mathbf{u})_{\Omega} + \Delta t\theta\{(\mathbf{v}, \rho^{\mathrm{f}}\mathbf{u}\cdot\nabla\mathbf{u})_{\Omega} + (\nabla\cdot\mathbf{v}, \boldsymbol{\sigma}^{\mathrm{f}})_{\Omega} \\
&\quad + (q, \nabla\cdot\mathbf{u})_{\Omega} - (\mathbf{v}, \boldsymbol{\lambda})_{\Gamma^+} - (\delta\boldsymbol{\lambda}, \mathbf{u})_{\Gamma^+}\}]^{n+1} \\
&\quad + [(\mathbf{v}^{\mathrm{ALE}}, \rho^{\mathrm{f}}\mathbf{u}^{\mathrm{ALE}})_{\Omega} + \Delta t\theta\{(\mathbf{v}^{\mathrm{ALE}}, \rho^{\mathrm{f}}(\mathbf{u}^{\mathrm{ALE}} - \mathbf{u}^{\mathrm{g}})\cdot\nabla\mathbf{u}^{\mathrm{ALE}})_{\Omega} + (\nabla\cdot\mathbf{v}^{\mathrm{ALE}}, \boldsymbol{\sigma}^{\mathrm{f}})_{\Omega} \\
&\quad + (q^{\mathrm{ALE}}, \nabla\cdot\mathbf{u}^{\mathrm{ALE}})_{\Omega} - (\mathbf{v}^{\mathrm{ALE}}, \boldsymbol{\mu})_{\Gamma^+} - (\delta\boldsymbol{\mu}, \mathbf{u}^{\mathrm{ALE}})_{\Gamma^+}\}]^{n+1} \\
&\qquad = (\mathbf{v}, \rho^{\mathrm{f}}\mathbf{u}^{n})_{\Omega} + \Delta t(1-\theta)(\mathbf{v}, \rho^{\mathrm{f}}\dot{\mathbf{u}}^{n})_{\Omega} - \Delta t\theta(\delta\boldsymbol{\lambda}, \bar{\mathbf{u}}^{\mathrm{i},n+1})_{\Gamma^+} \\
&\qquad\quad + (\mathbf{v}^{\mathrm{ALE}}, \rho^{\mathrm{f}}\mathbf{u}^{\mathrm{ALE},n})_{\Omega} + \Delta t(1-\theta)(\mathbf{v}^{\mathrm{ALE}}, \rho^{\mathrm{f}}\dot{\mathbf{u}}^{\mathrm{ALE},n})_{\Omega} - \Delta t\theta(\delta\boldsymbol{\mu}, \bar{\mathbf{u}}^{\mathrm{i},n+1})_{\Gamma^+}
\end{aligned}
\tag{64}
$$

The resulting matrix equation is then given as

$$
\begin{bmatrix}
\mathbf{A}_{uu} & \mathbf{A}_{up} & -\mathbf{M}_{\lambda}^{\mathrm{T}} & \mathbf{0} & \mathbf{0} & \mathbf{0} & \mathbf{0} \\
\mathbf{A}_{pu} & \mathbf{A}_{pp} & \mathbf{0} & \mathbf{0} & \mathbf{0} & \mathbf{0} & \mathbf{0} \\
-\mathbf{M}_{\lambda} & \mathbf{0} & \mathbf{0} & \mathbf{D}_{\lambda} & \mathbf{0} & \mathbf{0} & \mathbf{0} \\
\mathbf{0} & \mathbf{0} & \mathbf{D}_{\lambda}^{\mathrm{T}} & \mathbf{0} & \mathbf{D}_{\mu}^{\mathrm{T}} & \mathbf{0} & \mathbf{0} \\
\mathbf{0} & \mathbf{0} & \mathbf{0} & \mathbf{D}_{\mu} & \mathbf{0} & -\mathbf{M}_{\mu} & \mathbf{0} \\
\mathbf{0} & \mathbf{0} & \mathbf{0} & \mathbf{0} & -\mathbf{M}_{\mu}^{\mathrm{T}} & \mathbf{A}_{uu}^{\mathrm{ALE}} & \mathbf{A}_{up}^{\mathrm{ALE}} \\
\mathbf{0} & \mathbf{0} & \mathbf{0} & \mathbf{0} & \mathbf{0} & \mathbf{A}_{pu}^{\mathrm{ALE}} & \mathbf{A}_{pp}^{\mathrm{ALE}}
\end{bmatrix}
\begin{bmatrix}
\mathbf{u} \\ \mathbf{p} \\ \boldsymbol{\lambda} \\ \mathbf{u}^{\mathrm{i}} \\ \boldsymbol{\mu} \\ \mathbf{u}^{\mathrm{ALE}} \\ \mathbf{p}^{\mathrm{ALE}}
\end{bmatrix}
=
\begin{bmatrix}
\mathbf{f}^{\mathrm{rhs}} \\ \mathbf{0} \\ \mathbf{0} \\ \mathbf{0} \\ \mathbf{0} \\ \mathbf{f}^{\mathrm{ALE,rhs}} \\ \mathbf{0}
\end{bmatrix}
\tag{65}
$$

The coupled fluid–fluid system is solved in a monolithic way, where we can condense out the interface displacements and are left with a smaller system

$$
\begin{bmatrix}
\mathbf{A}_{uu} & \mathbf{A}_{up} & \mathbf{M}_{\lambda}^{\mathrm{T}} & \mathbf{0} & \mathbf{0} \\
\mathbf{A}_{pu} & \mathbf{A}_{pp} & \mathbf{0} & \mathbf{0} & \mathbf{0} \\
\mathbf{M}_{\lambda} & \mathbf{0} & \mathbf{0} & \mathbf{M}_{\mu} & \mathbf{0} \\
\mathbf{0} & \mathbf{0} & \mathbf{M}_{\mu}^{\mathrm{T}} & \mathbf{A}_{uu}^{\mathrm{ALE}} & \mathbf{A}_{up}^{\mathrm{ALE}} \\
\mathbf{0} & \mathbf{0} & \mathbf{0} & \mathbf{A}_{pu}^{\mathrm{ALE}} & \mathbf{A}_{pp}^{\mathrm{ALE}}
\end{bmatrix}
\begin{bmatrix}
\mathbf{u} \\ \mathbf{p} \\ \boldsymbol{\lambda} \\ \mathbf{u}^{\mathrm{ALE}} \\ \mathbf{p}^{\mathrm{ALE}}
\end{bmatrix}
=
\begin{bmatrix}
\mathbf{f}^{\mathrm{rhs}} \\ \mathbf{0} \\ \mathbf{0} \\ \mathbf{f}^{\mathrm{ALE,rhs}} \\ \mathbf{0}
\end{bmatrix}
\tag{66}
$$

The resulting system matrix appears similar to matrices obtained in Mortar methods; however, both matrices $\mathbf{M}_{\lambda}$ and $\mathbf{M}_{\mu}$ are rectangular.

The displacement of the fluid–fluid interface as well as the ALE mesh is arbitrary and its solution is not part of the coupled system given above. The mesh deformation can therefore be determined independently in a mesh smoothing step as in standard ALE methods.

If the structural deformation is mainly a rotational or translational one with only minor deformation of the structure, an attached fluid mesh around the structure provides a reliable alternative

DOI: 10.1002/fld

to the more general adaptive procedure presented in the previous section. For many applications such as spinning rotors or large translational motions of objects, this property does not pose a limitation. The presented approach has the additional advantage that, unlike Chimera methods, the coupled fluid–fluid system can be solved monolithically. This would then allow both iterative and monolithic FSI coupling schemes.

6. NUMERICAL EXAMPLES

In the following section, we present simulations to exemplify the proposed improvements. Since we were mainly concerned about the representation of the interface on the fixed-fluid grid and to keep the presentation clear, we neglect the structure in the first two examples and concentrate on fluid solution. However, as the approaches have been developed for FSI and have been implemented in a respective environment we will realize these examples as FSI problems with very stiff and properly fixed structures. Finally, a third example featuring FSI with deformable and compressible structure demonstrates the principle equivalence of ALE-based and adaptive XFEM/LM-based results.

For postprocessing purpose of scalar views, the intersected elements are shown using triangular integration cells. They solely serve to properly display the sharp interface in the postprocessing tool. Standard elements would display only a smeared solution, because the postprocessor has no information about the enrichment functions. nine-node bi-quadratic fluid elements without an intersecting solid boundary are displayed as four quadrilateral, bi-linear 4-node elements.

As a test case we compute the stationary flow around a cylinder, which is the first benchmark case as defined [28].

6.1. Adaptive fixed-grid method

The initial mesh was built from 4×24 bi-quadratic elements. Hence, the initial mesh consisted of 96 elements. The mesh was refined 5 times, after each refinement the solution of the fluid system was repeated. The final mesh consisted of 2740 fluid elements

For the refinement indicator, the strategy from Section 4 was used. Along the implicit interface, the refinement level was increased each adaptive step by 1. In addition, a number of elements were refined, where high gradients are observed.

The final result can be seen in Figure 6. The velocity component u_x of the fluid solution is shown over the whole fluid domain in Figure 6(b) and near the interface in Figure 7. Intersected elements are shown using the integration cells, where fluid integration cells within the structural domain have been removed from the plot.

Figure 6 shows the finest mesh that we used to study this problem. With this, we could already achieve very good agreement with the averaged results given in [28]. In particular, we calculated $c_{\mathrm{L}}=0.0054$ for the lift, $c_{\mathrm{D}}=5.5624$ for the drag and $\Delta p^{\mathrm{f}}/\rho=0.1172\,\mathrm{m}^2/\mathrm{s}^2$ for the normalized pressure difference.

The benchmark clearly shows the potential gains in efficiency along with adaptive meshing when using fixed-grid methods for the fluid domain.

6.2. Stationary flow around a cylinder using the hybrid approach

For this simulation we use the same setup as in the first example. In this example, we prescribed an initial refinement for all elements in the entrance part of the channel to calculate a good solution

DOI: 10.1002/fld

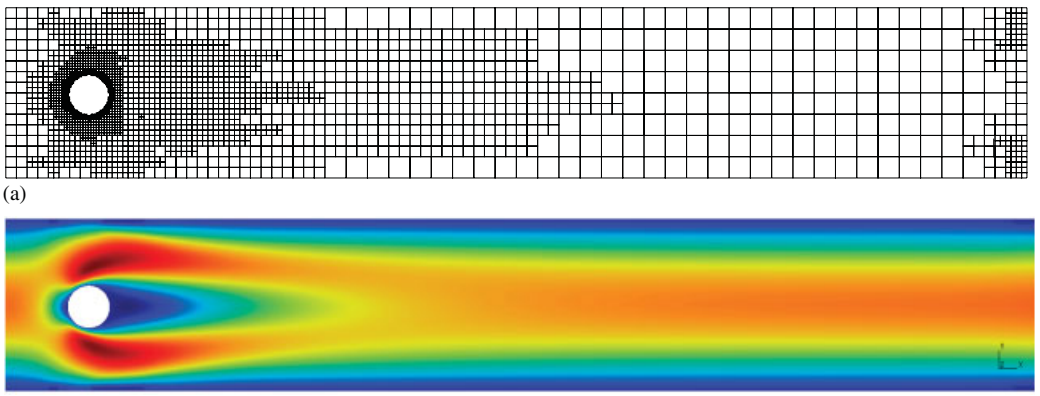

Figure 6. CFD benchmark: Finest mesh used to calculate lift and drag values on the cylinder. It consists of 284 linear Lagrange multiplier elements and 2740 quadratic 9-node fluid elements. (a) Maximal refinement used in computation and (b) shows the x-component of the velocity field. The structure is not displayed.

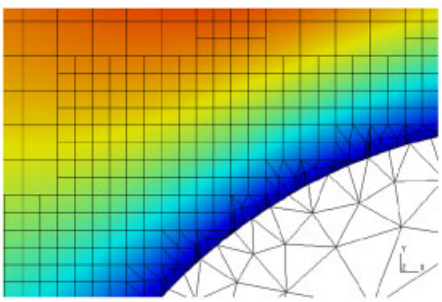

Figure 7. x-component of the velocity field near the interface. In the structural domain (lower right corner), the structural mesh is displayed. In the fluid domain, near the interface, triangular integration cells are used for visualization and numerical integration.

away from the structure. Instead of refining the mesh near the cylinder surface as before, we used the proposed hybrid approach. The final solution can be seen in Figure 8. The velocity component u_x of the fluid solution is shown over the whole fluid domain in Figure 8(a) and near the interface in Figure 8(b).

The surface-fitted mesh much closely resembles the boundary layer near the cylinder surface and the boundary layer can be resolved much more efficiently. Of course, the hybrid approach can be combined with the aforementioned h-adaptivity. As mentioned before, for high Reynolds number flows optimal state-of-the-art techniques for resolving boundary layers such as high aspect ratio elements can be used. Here, the hybrid approach could potentially outperform adaptivity by element subdivision. We currently extend the formulation to 3d, which eventually might allow a more detailed performance comparisons for realistic applications.

DOI: 10.1002/fld

6.3. *FSI including a compressible structure*

The final example demonstrates a simple validation of the XFEM/LM approach by comparing it with computations performed by a state-of-the-art partitioned, iterative ALE-based FSI solver as described in [29].

The principle setup of the problem is depicted in Figure 9(a). The structure has initially a circular shape and is then compressed by the flow field. The material parameters for a St-Vernant Kirchhoff material law are Poisson's ratio $\nu = 0.0$ and an elastic modulus $E = 50$. The fluids' kinematic viscosity and density are set to 1, respectively. The setup and the solution should be symmetric. The structure was fixed such that the rigid body modes were constrained without constraining the expected symmetric deformation with respect to the x- and the y-axis.

The fluid field in both solutions was discretized with equal-order, bi-quadratic 9-node elements using identical stabilization as described in [4]. In the ALE approach, matching grids were used

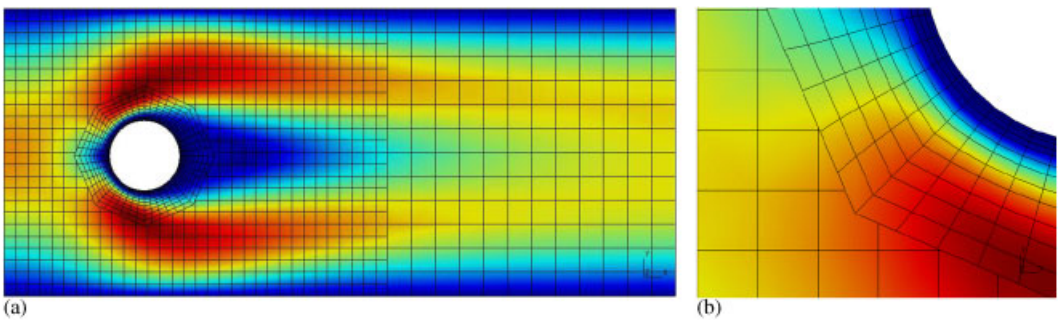

Figure 8. CFD benchmark using the hybrid approach: The initial mesh was refined in the inflow region and in addition, an fluid mesh patch surrounding the structure is applied: (a) x-component of the velocity field and (b) close up view.

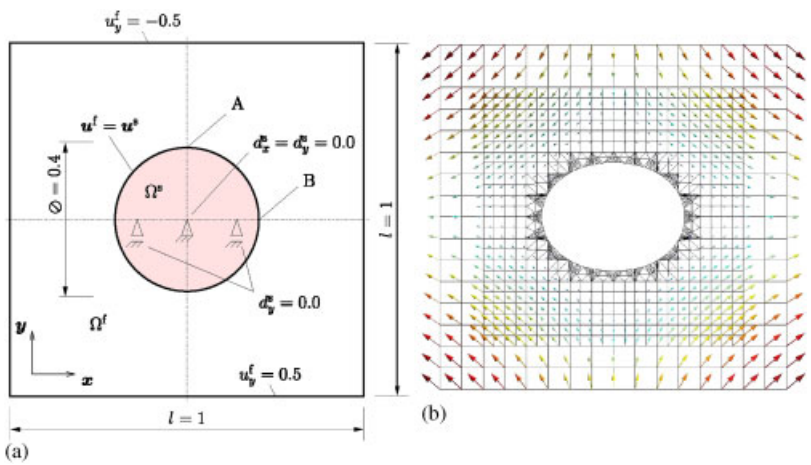

Figure 9. Setup (a) and principle solution (b) of the compressible cylinder example.

DOI: 10.1002/fld

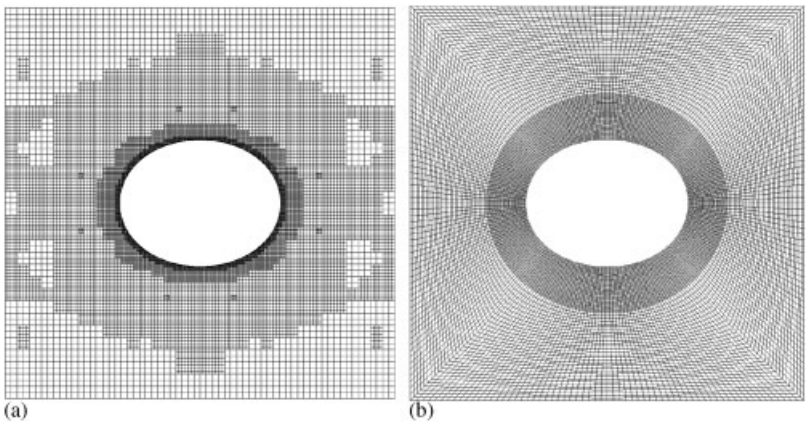

Figure 10. Final meshes used for comparison: (a) adaptively refined XFEM mesh and (b) ALE mesh.

between fluid and solid surface and the structure was discretized with 2698 quadratic, triangular 6-node elements. In the XFEM computation, about 1294 linear triangular 3-node elements were used.

For the ALE computation, the mesh was refined *a priori* and the FSI computation was performed for each mesh until convergence to a final structure deformation. During the solution with the XFEM-based approach, a steady-state solution was carried out, where after two FSI iterations a refinement by subdivision of 20% of the active fluid elements was performed. The solution was transferred to the newly created nodes and used as the starting field for the next two FSI iterations. Eventually, six refinement levels were performed until no changes in the structural deformation between subsequent refinement levels were observable. The final mesh consisted of 17 860 active elements (elements in the fluid domain or intersected elements) with about 23 000 unknowns (fluid velocity, pressure and Lagrange multipliers combined). Note that the initial mesh consisted of only 16 (4×4) fluid elements.

The meshes used for comparison are shown in Figure 10. The maximal displacement was observed at the top and the bottom (Point A) of the structure at $x=0.5$. Point A moved by $u_y^{\mathrm{A}}=-0.0379$. Point B had a displacement of $u_x^{\mathrm{B}}=0.00663$. ALE and XFEM computations differed by less then 0.01% in the maximal structure displacement. Other measures compared equally well. The area occupied by the structure changed significantly by about 16.3% when compared with the original area.

Using two completely different discretization and coupling approaches, the very good agreement gives confidence that both the automatic adaptive refinement and the presented hybrid approach lead to accurate FSI solutions. While no stability issues were encountered during the numerical examples, a detailed mathematical stability analysis of the interface description is still missing.

7. CONCLUSION

In this paper we have discussed ways of further improving fixed-grid methods. We used fluid–structure problems as an example for such moving interface fixed-grid flow problems. Fixed-grid

DOI: 10.1002/fld

methods for FSI are subject to a growing number of current research undertaken. The ultimate goal is to remove the burden of fluid mesh movement and, if deformation of the structure becomes excessive, re-meshing. For that purpose, we developed a fixed-grid method in [4] that allows an accurate treatment of the interface description on the fixed grid and the coupling to the structure.

We discussed two ways of improving the resolution of the fluid solution near the interface. The first approach uses local adaptivity by element subdivision. We avoided re-meshing techniques, since fixed-grid methods were developed to exactly avoid the re-meshing needed in ALE methods during large deformation. Hanging nodes were constrained to achieve compatible meshes. Heuristic and error-based indicators can be used to determine regions for refinement and coarsening, which we demonstrated with the given examples.

The second approach is a hybrid fixed-grid/ALE technique where an ALE mesh surrounds the structure to enhance the solution near the interface. It allows the application of state-of-the-art boundary layer techniques while still keeping large flexibility with respect to the possible deformation the structure can undergo. For boundary layers, typically elements with high aspect ratios are used. Such optimal meshes cannot be achieved by element subdivision, if the interface is not aligned with the element surfaces. Especially for this approach we showed how this can very elegantly be realized in the same spirit as our recently introduced XFEM/LM scheme [4]. This new approach also allows for a number of interesting new options such as, e.g. simple ways of introducing special enrichment functions near the interface.

It remains to be shown, which techniques prove most useful, when fixed-grid methods are applied to real-world applications. Further developments currently concentrate on an efficient 3d implementation using parallel algorithms and a combination of techniques as described in this paper to eventually apply fixed-grid methods to real-world applications.

ACKNOWLEDGEMENTS

The present study is supported by a grant of the 'Deutsche Forschungsgemeinschaft' (DFG) through project WA 1521/1 within DFG's Research Unit 493 'FSI: Modelling, Simulation, and Optimization'. This support is gratefully acknowledged.

REFERENCES

1. Wall WA, Gerstenberger A, Gamnitzer P, Förster C, Ramm E. Large deformation fluid–structure interaction—advances in ALE methods and new fixed grid approaches. In *Fluid–Structure Interaction*: *Modelling*, *Simulation*, *Optimisation*, Bungartz H-J, Schäfer M (eds). Lecture Notes in Computational Science and Engineering. Springer: Berlin, 2006.
2. Tezduyar TE, Sathe S. Modelling of fluid–structure interactions with the space–time finite elements: solution techniques. *International Journal for Numerical Methods in Fluids* 2007; **54**(6–8):855–900.
3. Wall WA, Gamnitzer P, Gerstenberger A. Fluid–structure interaction approaches on fixed grids based on two different domain decomposition ideas. *International Journal of Computational Fluid Dynamics* 2007; submitted.
4. Gerstenberger A, Wall WA. An extended finite element method/Lagrange multiplier based approach for fluid–structure interaction. *Computer Methods in Applied Mechanics and Engineering* 2008; DOI:10.1016/j.cma.2007.07.002.
5. Förster C, Wall WA, Ramm E. On the geometric conservation law in transient flow calculations on deforming domains. *International Journal for Numerical Methods in Fluids* 2006; **50**(12):1369–1379.
6. Förster C, Wall WA, Ramm E. Artificial added mass instabilities in sequential staggered coupling of nonlinear structures and incompressible viscous flows. *Computer Methods in Applied Mechanics and Engineering* 2007; **196**(7):1278–1293.

DOI: 10.1002/fld

7. Belytschko T, Black T. Elastic crack growth in finite elements with minimal remeshing. *International Journal for Numerical Methods in Engineering* 1999; **45**(5):601–620.
8. Moës N, Dolbow J, Belytschko T. A finite element method for crack growth without remeshing. *International Journal for Numerical Methods in Engineering* 1999; **46**(1):131–150.
9. Babuška IM, Melenk JM. The partition of unity method. *International Journal for Numerical Methods in Engineering* 1997; **40**(4):727–758.
10. Moës N, Béchet E, Tourbier M. Imposing Dirichlet boundary conditions in the extended finite element method. *International Journal for Numerical Methods in Engineering* 2006; **67**(12):1641–1669.
11. Bernardi C, Maday Y, Patera AT. Domain decomposition by the mortar element method. In *Asymptotic and Numerical Methods for Partial Differential Equations*, Kaper H *et al*. (eds), vol. 384, Reidel, Dordrecht, 1993; 269–286.
12. Bernardi C, Maday Y, Patera AT. A new nonconforming approach to domain decomposition: the mortar element method. In *Nonlinear Partial Differential Equations and their Applications*, Brezzi H *et al*. (eds), vol. 299, Paris, 1994; 13–51.
13. Wohlmuth BI. *Discretization Methods and Iterative Solvers Based on Domain Decomposition*. Springer: Berlin, 2001.
14. Belytschko T, Liu WK, Moran B. *Nonlinear Finite Elements for Continua and Structures*. Wiley: New York, 2000.
15. Hughes TJ, Liu WK. Implicit–explicit finite elements in transient analysis. *Journal of Applied Mechanics* 1978; **45**:371–378.
16. Solin P, Cerveny J, Dolezel I. Arbitrary-level hanging nodes and automatic adaptivity in the hp-fem. *Mathematics and Computers in Simulation*, 2007; DOI: 10.1016/j.matcom.2007.02.011.
17. Oñate E, Arteaga J, García J, Flores R. Error estimation and mesh adaptivity in incompressible viscous flows using a residual power approach. *Computer Methods in Applied Mechanics and Engineering* 2006; **195**(4–6):339–362.
18. Sahni O, Müller J, Jansen K, Shephard M, Taylor C. Efficient anisotropic adaptive discretization of the cardiovascular system. *Computer Methods in Applied Mechanics and Engineering* 2006; **195**(41–43):5634–5655.
19. Zienkiewicz OC, Zhu JZ. The superconvergent patch recovery and *a posteriori* error estimates. Part 1: the recovery technique. *International Journal for Numerical Methods in Engineering* 1992; **33**(7):1331–1364.
20. Zienkiewicz OC, Zhu JZ. The superconvergent patch recovery and *a posteriori* error estimates. Part 2: error estimates and adaptivity. *International Journal for Numerical Methods in Engineering* 1992; **33**(7):1365–1382.
21. Stein E, de Borst R, Hughes TJR (eds). *Encyclopedia of Computational Mechanics*. Wiley: New York, 2004.
22. Cougny HLD, Shephard MS. Parallel refinement and coarsening of tetrahedral meshes. *International Journal for Numerical Methods in Engineering* 1999; **46**(7):1101–1125.
23. Meakin RL, Suhs NE. Unsteady aerodynamic simulation of multiple bodies in relative motion. *AIAA Paper 89-1996-CP*.
24. Steger JL, Dougherty FC, Benek JA. A Chimera grid scheme. In *Advances in Grid Generation*, Ghia KN, Ghia U (eds), vol. 5. ASME, FED: New York, 1983.
25. Wang ZJ, Parthasarathy V. A fully automated Chimera methodology for multiple moving body problems. *International Journal for Numerical Methods in Fluids* 2000; **33**(7):919–938.
26. Gamnitzer P, Wall WA. An ALE-chimera method for large deformation fluid structure interaction. In *European Conference on Computational Fluid Dynamics*, *ECCOMAS CFD 2006*, Wesseling P, Oñate E, Périaux J (eds), TU Delft, 2006.
27. Behr M, Tezduyar TE. The shear-slip mesh update method. *Computer Methods in Applied Mechanics and Engineering* 1999; **174**:261–274.
28. Schäfer M, Turek S. *Benchmark Computations of Laminar Flow Around a Cylinder*. Notes on Numerical Fluid Mechanics, Hirschel EH (ed.), vol. 52, Vieweg, 1996; 547–566.
29. Küttler U, Wall WA. Fixed-point fluid–structure interaction solvers with dynamic relaxation. *Computational Mechanics* 2008; DOI: 10.1007/s00466-008-0255-5.